


Mapping Transport Properties of Halide Perovskites via Short-Time-Dynamics Scaling Laws and Subnanosecond-Time-Resolution Imaging

Guillaume Vidon^{1,2,*}, Stefania Cacovich^{1,2}, Marie Legrand^{1,3}, Armelle Yaiche^{1,3}, Daniel Ory^{1,3}, Daniel Suchet^{1,2}, Jean-Baptiste Puel^{1,3} and Jean-François Guillemoles^{1,2,†}

¹IPVF, Institut Photovoltaïque d'Ile-de-France, 18 Boulevard Thomas Gobert, Palaiseau 91120, France

²Institut Photovoltaïque d'Ile de France, UMR IPVF 9006, CNRS, Ecole Polytechnique, Institut Polytechnique de Paris, PSL Chimie ParisTech, IPVF SAS, Palaiseau 91120, France

³EDF R&D, 18 Boulevard Thomas Gobert, Palaiseau 91120, France

 (Received 9 March 2021; revised 30 August 2021; accepted 28 September 2021; published 29 October 2021)

The excellent optoelectronic and transport properties of halide perovskites have led to the rapid development of perovskite-based optoelectronic devices. A fundamental understanding of charge-carrier dynamics, as well as the implementation of physical models able to accurately describe their behaviour, is essential for further improvements in the field. Here, combining advanced modeling and characterization, a method for analyzing the short time dynamics of time-resolved fluorescence imaging (TRFLIM) decays is demonstrated. A theoretical scaling law for the time derivative of transient photoluminescence decays as a function of excitation power is extracted. This scaling law, computed from classical drift-diffusion equations, defines an innovative and simple way to extract quantitative values for several transport parameters, including the external radiative-recombination coefficient. The model is notably applied on a set of images acquired with a temporal shift of 250 ps to map the top-surface recombination velocity of a triple-cation mixed-halide perovskite thin film at the microscale. The development of high-time-resolution imaging techniques coupled with a scaling method for analyzing short time dynamics provides a solid platform for the investigation of local heterogeneities in semiconductor materials and the accurate determination of the main parameters governing their carrier transport.

DOI: [10.1103/PhysRevApplied.16.044058](https://doi.org/10.1103/PhysRevApplied.16.044058)

I. INTRODUCTION

Over the last decade, lead-halide perovskites solar cells have proved to be a serious candidate for reaching large-scale photovoltaic solar-energy conversion, a much-needed solution to meet climate targets and move towards a low-carbon economy. However, despite this emerging technology having recently reached a record power conversion efficiency of 25.5% for a single-junction device [1,2], several open questions persist in the scientific community, ranging from the nature and densities of the defects in the absorbers [3–5] to the optimal design for interface energetics in a full device [6,7] and long-term stability [7–9].

The optimization of device performances goes along with a complete understanding of complex recombination processes occurring both in the bulk and at interfaces. Due to the interplay of several chemical and physical parameters in these hybrid compounds, such studies often require the use of advanced characterization methods. Among these, time-resolved photoluminescence (TRPL)

is widely used to probe halide-perovskite transport properties [10,11]. If the TRPL experiments are rather easy to perform, difficulties lie in the correct physical interpretation of the signal [12,13]. To date, two main approaches are employed in the literature: one based on phenomenological fitting of the decays and the other on the use of drift-diffusion equations. In the first case, fitting functions, such as monoexponential, biexponential [14], stretched exponential [7,15,16], and triexponential [17], are arbitrarily chosen. Though fitting the decays with these custom chosen functions often yields close correspondence with the observed signal, the fitted time constants and parameters have no strict physical meaning. The second method relies on a microscopic drift-diffusion model to describe the dynamics of carrier transport and recombination [18–23]. This approach is also employed as the basis for the development of more complex models, with the aim of investigating in-depth diffusion [19,24] or photon recycling [25,26]. However, this interpretation method has multiple drawbacks. First of all, these models assess a large number of microscopic parameters from the fitting of a handful of decays, such as the diffusion coefficient, recombination rate constants, interface properties, and device geometry. Therefore, questions arise about the

*guillaume.vidon@ipvf.fr

†jean-francois.guillemoles@cnrs.fr

number of independent parameters that can be determined with this method. Another major drawback stems from the fact that multiple sets of parameters can account satisfyingly for the same measured signal [27]. Moreover, uncertainty computations are not often detailed, and the correlation between fitted parameters are rarely reported. Another important issue concerns the treatment of large datasets acquired by time-resolved imaging setups, such as time-resolved fluorescence imaging (TRFLIM). Indeed, fitting decays with drift-diffusion models can be time-consuming, and therefore, performing fits for every pixel of an image requires intense computational power. Thus, to accurately map local transport parameters, alternative approaches in modeling and data treatment are required.

Here, we establish a theoretical relationship that allows for the direct determination of physical parameters without using drift-diffusion fitting. This method directly outputs coefficients that are related to physical parameters via theoretical formulae. Our approach is based on a scaling law we derive for the time derivative of the transient PL signal computed just after the laser pulse. Other groups use the derivative of the PL signal to describe different physical phenomena. For instance, Krogmeier and co-workers [28] defined a differential lifetime of a halide perovskite closely linked with such a derivative [18]. Saba and co-workers displayed the initial derivative as a function of laser fluence studied on methylammonium (MA) lead triiodide (MAPbI₃) and MAPbI_{3-x}Cl_x perovskite [29]. However, in only a few publications [21,30] were the theoretical components of the PL derivative directly associated with their physical origin, i.e., carrier diffusion and recombination in the bulk or at interfaces via traps and radiative recombination. In these publications, the derivative is computed in a general and thus integral form. As no specific analytical form for the inhomogeneous photogenerated carrier-density profile, $\Delta n(z, t)$, is considered, the integrals are not computed.

We propose to compute the expected derivative and integrals a “short time” after the pulse, when one can make an assumption about the photogenerated carrier-density spatial profile based on Beer-Lambert’s law. We obtain a law that is linear in laser fluence. Starting from this law and from the observation of the short time derivative of the PL signal, it is possible to extract accurate values of physical parameters, such as the external radiative-recombination coefficient or top-surface recombination velocity. This method can also be applied for the analysis of three-dimensional datasets, acquired with both imaging systems and confocal PL setups, although a very precise signal is needed for local application. One of the benefits of considering only the beginning of the decays is found in the high signal-to-noise ratio of the curves in this temporal window.

This paper is arranged as follows. We first discuss the theoretical approach we use to derive the scaling law at a short time. Then, we experimentally validate the model

by determining the main transport parameters of a state-of-the-art triple-cation lead-halide perovskite thin film. Using this dataset, we show that this technique allows the transport properties, such as the top-surface recombination velocity, to be accurately mapped. Finally, we comment on the range of validity of the technique, as well as on the quality of its output-parameter values, and compare this approach to the usual drift-diffusion fitting technique to highlight their complementarity.

II. MODEL DESCRIPTION

A. The drift-diffusion model

In this section, we introduce the theoretical concepts leading to the scaling law we establish. The first hypothesis we make is to tackle the case of intrinsic materials. We consider a slab of intrinsic semiconductor material of thickness L . As the material is intrinsic, and the electric field is not considered, we assume that the electron and hole local densities are equal at any time and position, meaning $n_e(z, t) = n_h(z, t) \equiv n(z, t)$. The sample is illuminated by a pulsed laser from its top surface. The pulse duration of the laser used later in this study is in the order of tens of picoseconds. However, the time resolution of the gates of the TRFLIM setup is in the order of nanoseconds; therefore, we model the pulse as an initial condition for the excess carrier density, $\Delta n(z, t)$, and not as a time-dependent generation function. This kind of approximation has been previously used in the literature, for instance, by Maiberg and Scheer [21]. For the initial spatial profile of the excess carrier density, we assume Beer-Lambert’s law:

$$\Delta n(z, t = 0) = n_\gamma \alpha e^{-\alpha z}, \quad (1)$$

with n_γ as the fluence of the laser in ph cm^{-2} per pulse and α in cm^{-1} as the absorption coefficient of the material at the excitation wavelength, λ , of the laser.

From this initial state, the system will relax towards the equilibrium solution, $\Delta n = 0$. The drift-diffusion equation is used to describe this relaxation. We write it in the following form, which is valid at each position z inside the absorber and time $t > 0$ [31]:

$$\frac{\partial \Delta n}{\partial t}(z, t) = D \frac{\partial^2 \Delta n}{\partial z^2}(z, t) - R(z, t), \quad (2)$$

with D as the diffusion coefficient in $\text{cm}^2 \text{s}^{-1}$, and $R(z, t)$ as the recombination rate in $\text{cm}^{-3} \text{s}^{-1}$ at position z and time t . We consider two main types of bulk recombination: recombination via traps or Shockley-Read-Hall (SRH) recombination [32,33] and radiative recombination. The recombination rate is therefore

$$R = k_1 \frac{(\Delta n)^2}{\Delta n + N_{\text{bulk}}} + k_2 (\Delta n)^2, \quad (3)$$

where we introduce the nonradiative recombination rate coefficient, k_1 , in s^{-1} and the external radiative recombination rate coefficient, k_2 , in $\text{cm}^3 \text{s}^{-1}$. N_{bulk} accounts for the case of defects that have an energy close to one of the bands; see more details in Sec. 1.1 within the Supplemental Material [34]. Notably, in Eq. (3), the intrinsic carrier density, n_i , is neglected with respect to Δn , leading us to approximate $n^2 - n_i^2 \approx \Delta n^2$.

While photon recycling is shown to play an important role for thick perovskite absorbers [35,36], the impact of this process on thin films is still under debate. One way to take photon recycling into account is by introducing a factor applied to the internal radiative recombination coefficient [37], namely, $k_2 = p_{\text{esc}} k_2^{\text{int}}$, with $p_{\text{esc}} < 1$ being the probability of escape for a photon, and k_2^{int} as the internal radiative-recombination coefficient. A more advanced way of modeling was proposed by Ansari-Rad and Bisquert, who considered an effective drift-diffusion equation for photons coupled with those of the carriers [38]. We use their model to evaluate the impact of photon recycling and light outcoupling in the case under study. The details are presented in Sec. I.E within the Supplemental Material [34]. The main conclusion is that photon recycling plays almost no role in the present case because we consider thin layers relative to the absorption length at the emission wavelength. It could, however, in other cases, have an impact by modifying the observed external radiative-recombination coefficient. We therefore leave k_2 to represent the external radiative-recombination coefficient for a general model, even though our experimental conditions correspond to a case where it close to the internal radiative-recombination coefficient.

Auger recombination is not considered, as it is relevant only at very high carrier densities, $> 10^{17} \text{ cm}^{-3}$, at least for MAPbI_3 perovskites [39]. However, as detailed in Sec. I.D within the Supplemental Material [34], Auger terms can be taken into account. Our observations conclude that they are negligible in the case under study.

From the definition of the radiative-recombination rate, we can set the PL intensity received by the detector at time t as

$$I_{\text{PL}}(t) = A \int_0^L \Delta n^2(z', t) dz', \quad (4)$$

with A being a proportionality factor that describes the precise losses and geometry of the measurement setup.

Recombination processes occurring at the interfaces are proved to critically affect device performance [40,41]. We thus introduce surface recombination at the top and bottom interfaces into the model. At the top interface,

$$D \frac{\partial \Delta n}{\partial z}(z = 0, t) = S_{\text{top}} \frac{\Delta n(z = 0, t)^2}{\Delta n(z = 0, t) + N_{\text{top}}}, \quad (5)$$

where S_{top} is the top-surface recombination velocity, and N_{top} is the corresponding defect-related density, similar to N_{bulk} . A similar expression (with a minus sign) is considered at the bottom interface at $z = L$, with S_{bot} being the bottom-surface recombination velocity and N_{bot} as the corresponding defect-related density.

B. The scaling law a short time after the pulse

Guided by the fact that all driving forces are present at the initial time, we compute analytically the time derivative shortly after the pulse of the PL signal normalized by its maximum value:

$$\left. \frac{dI_{\text{PL}}^{\text{norm}}}{dt} \right|_{t=0} = \frac{1}{I_{\text{PL}}(t=0)} \left. \frac{dI_{\text{PL}}}{dt} \right|_{t=0}. \quad (6)$$

To go further, we make the following and main approximation. We assume that, shortly after the pulse, the carrier density is both close to its initial Beer-Lambert-like state and all the while respecting the drift-diffusion equation. Using this approximation, along with the definition of the PL [Eq. (4)] and the drift-diffusion equation [Eq. (2)], one can compute the theoretical value of Eq. (6). A general form can be computed, as demonstrated in Sec. 1.2 within the Supplemental Material [34]. This extended form can be further simplified with additional assumptions: (i) the excitation wavelength is strongly absorbed ($e^{-\alpha L} \ll 1$) and (ii) the defect-related densities are negligible compared to the excitation densities ($n_\gamma \alpha \gg N_{\text{bulk}}, N_{\text{top}}$). More details on the approximation validity are given in Sec. I.B within the Supplemental Material [34]. Under such approximations, we obtain the following scaling law:

$$\left. \frac{dI_{\text{PL}}^{\text{norm}}}{dt} \right|_{t=0} = -2 [k_1 + \alpha^2 D + 2\alpha S_{\text{top}}] - \frac{4}{3} [k_2 \alpha] n_\gamma. \quad (7)$$

This equation relates the derivative of the normalized decay curve just after the laser pulse to the model parameters, notably, to the experimentally accessible parameters: the fluence, n_γ , and the laser-wavelength-dependent absorption coefficient, $\alpha(\lambda)$. The slope of this linear behavior gives direct access to the product αk_2 . The absorption coefficient can be measured via other methods, such as Fourier-transform photocurrent spectroscopy [42,43] or ellipsometry [44]. Therefore, one can extract a direct measurement of the external radiative-recombination rate, k_2 . The intercept of the scaling gives direct access to the quantity $k_1 + \alpha^2 D + 2\alpha S_{\text{top}}$. There is a major difference between the intercept of the scaling at a short time and the (long-time) observed lifetime: the spatial distribution of the carriers. For the short-time intercept, it follows Beer-Lambert's law, while for the lifetime a more homogeneous distribution is reached (not entirely homogeneous due to surface recombination). These two distributions explain

the difference, in terms of theoretical formulae, between these two characteristic times of the system.

Equation (7) suggests two sets of experiments. The first one consists of measuring decays when varying the laser fluence at a given laser wavelength. This approach is widely employed in the literature [20,22,24,28]. In this case, one could explore how the initial slopes of the relative decays exhibit a linear relationship with laser fluence. The other set of experiments would consist of varying the laser wavelength at fixed laser fluence. Then, as long as the high-absorption condition, $e^{-\alpha L} \ll 1$, is fulfilled, one expects a polynomial of second order in α for the initial derivative (a generalized version of the scaling for the low-absorption case is given in Sec. I.F within the Supplemental Material [34]). Combining the two methods would give access to most of the model parameters, k_1 , D , S_{top} , and k_2 , without the use of any complex numerical models. This second set of experiments will be the subject of a future study, while we will tackle fluence-dependent studies in the rest of this paper.

III. EXPERIMENTAL RESULTS ON TRIPLE-CATION PEROVSKITE

To validate the proposed model, we perform TRFLIM experiments on triple-cation perovskite thin films [$\text{Cs}_{0.05}(\text{MA}_{0.17}\text{FA}_{0.83})_{0.95}\text{Pb}(\text{Br}_{0.17}\text{I}_{0.83})_3$; FA, formamidinium] deposited on glass substrates. Acquisitions are carried out by applying a wide-field pulsed illumination ($\lambda = 532$ nm) under a protective N_2 atmosphere at a temperature of 20°C to prevent light-soaking effects [45]. Each acquisition is repeated 3 times and good reproducibility is obtained, as reported in Fig. S2 within the Supplemental Material [34]. We acquire images with a 3-ns-long exposure gate. To further improve the time resolution of our measurement, we acquire one image every 250 ps during 19.5 ns, see Fig. 1(a). Thus, we obtain subnanosecond-resolved images and decays. One of the advantages of the subnanosecond-resolved curves is that they allow verification that the maximum of the PL decay is not missed by a desynchronization between the laser pulse and the gated camera, which is critical when normalizing decays. However, for such temporal resolution, it is necessary to consider the convolution of the signal with the camera's temporal-response function. We also acquire *regular* data cubes, by taking one image every 3 ns from $t = -21$ to 879 ns, as shown in the inset of Fig. 1(b).

In Fig. 1(b), we plot subnanosecond-resolved decays acquired at different laser fluences (varying from 4×10^{11} to 1×10^{13} ph cm^{-2}) and averaged over the whole image. The corresponding scaling is shown in Fig. 1(c), as blue dots. The derivative is computed as the slope of a linear fit of the natural logarithm of the PL between 0.5 and 2.5 ns. Two datasets are considered: in the former, the derivative is performed on the raw decays shown in Fig. 1(b),

while in latter we compute the derivative on the results of a deconvolution algorithm applied to the decays. The deconvolution algorithm uses a Wiener filter and is described in Sec. 3 within the Supplemental Material [34], along with the resulting decays. To correctly evaluate the deconvolution, we measure our apparatus-response function and use fast-Fourier-transform algorithms to recover the original signal. A parameter, denoted K , is needed for the Wiener-filter deconvolution and is taken here to be $K = 0.1$. Its influence is discussed in Sec. 3 within the Supplemental Material [34]. We also test a third method of deconvolution, via an effective fit of a convolved biexponential with results close to the Wiener deconvolution. Details are given in the Supplemental Material [34]. For both scalings, linear behavior for the initial derivative with the laser fluence is observed, as expected from Eq. (7). Then, we fit linearly the points of Fig. 1(c), to obtain the slope $a = -4/3\alpha k_2$ and intercept $b = -2[k_1 + \alpha^2 D + 2\alpha S_{\text{top}}]$ of the scaling law. For the raw dataset, we obtain values of $a = -(5.7 \pm 0.6) \times 10^{-6} \text{ cm}^2 \text{ s}^{-1}$ and $b = -(1.24 \pm 0.03) \times 10^8 \text{ s}^{-1}$, whereas for the deconvoluted dataset we find $a = -(1.07 \pm 0.15) \times 10^{-5} \text{ cm}^2 \text{ s}^{-1}$ and $b = -(2.06 \pm 0.08) \times 10^8 \text{ s}^{-1}$.

We can make three remarks on the impact of temporal convolution. (i) The order of magnitude of the parameters is similar for both results after and before deconvolution. (ii) Characterizing the apparatus-response function allows the use of deconvolution algorithms; these algorithms are especially efficient in the high signal-to-noise regions, which is exactly our temporal window of interest when computing the short time derivative. (iii) The use of deconvolution algorithms is necessary because the characteristic timescales of the material's decay are comparable to the temporal resolution of our camera. We want to stress that deconvolution would not be necessary for the study of materials with longer characteristic timescales.

Furthermore, we use the results from the deconvoluted dataset [$k_2 \alpha_{532 \text{ nm}} = (8.0 \pm 1.1) \times 10^{-6} \text{ cm}^2 \text{ s}^{-1}$] to estimate the transport parameters of the perovskite layer. Assuming an absorption coefficient at the laser wavelength (532 nm), $\alpha = (6.5 \pm 1) \times 10^4 \text{ cm}^{-1}$, from previous measurements, and in line with literature values for this composition and laser wavelength [35], we can extract the value of the external radiative-recombination coefficient, $k_2 = (1.2 \pm 0.4) \times 10^{-10} \text{ cm}^3 \text{ s}^{-1}$, by using Eq. (7). Moreover, we can provide lower and upper bounds for the multiple parameters expressed in the intercept coefficient. The bulk lifetime, $\tau = 1/k_1$, would, in this regard, be such that $\tau \geq 10$ ns, which is highly expected for triple-cation perovskites. The diffusion coefficient would be less than $D \leq 2.4 \times 10^{-2} \text{ cm}^2 \text{ s}^{-1}$, corresponding to a mobility of $\mu \leq 0.9 \text{ cm}^2 \text{ s}^{-1} \text{ V}^{-1}$ at ambient temperature. For the top-surface recombination velocity, one finds that $S_{\text{top}} \leq 790 \text{ cm s}^{-1}$. All of these conditions are in agreement with

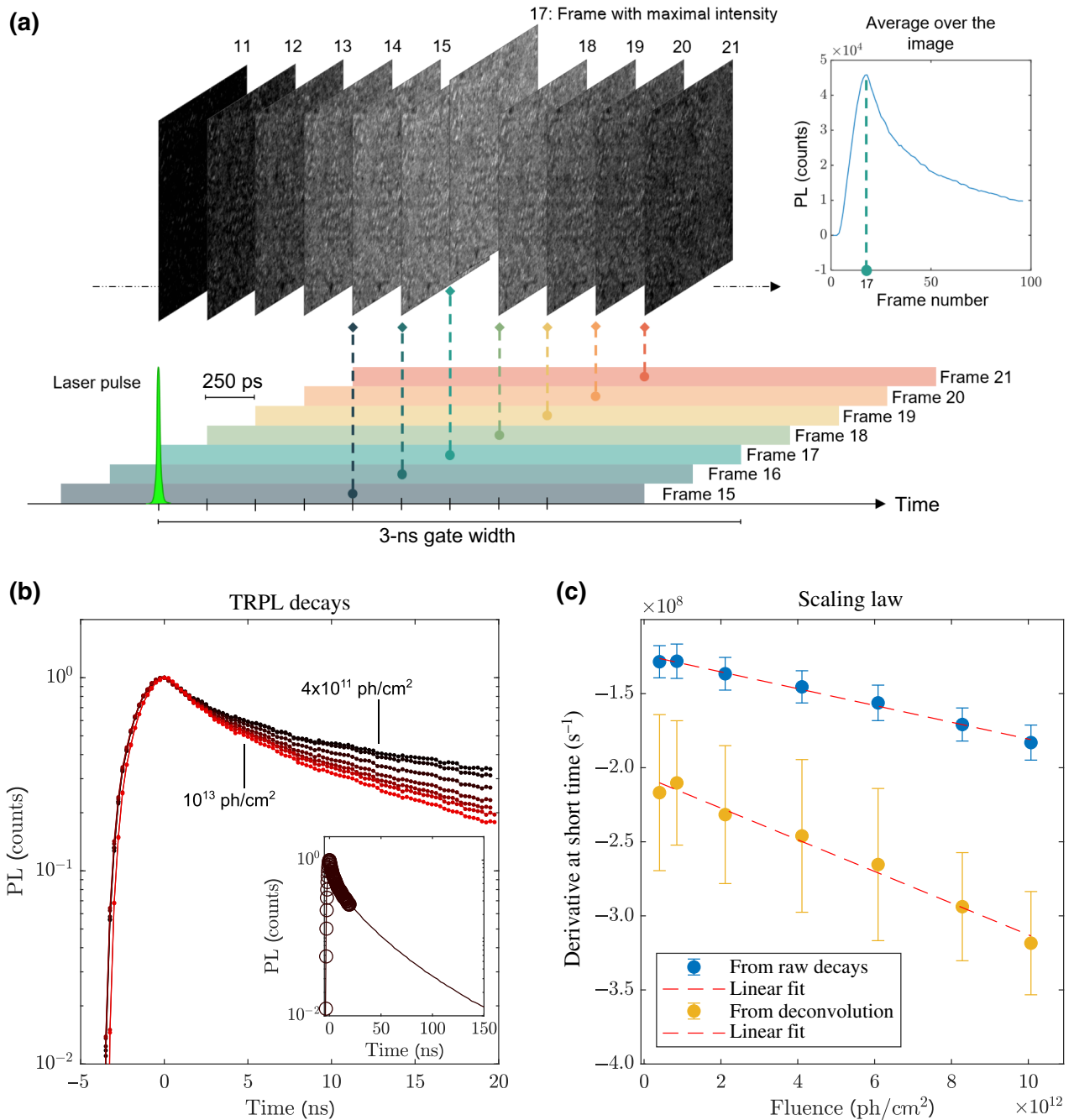


FIG. 1. Experiments on triple-cation perovskite $[\text{Cs}_{0.05}(\text{MA}_{0.17}\text{FA}_{0.83})_{0.95}\text{Pb}(\text{Br}_{0.17}\text{I}_{0.83})_3]$ thin films under an inert atmosphere. (a) Scheme of subnanosecond-resolved TRFLIM acquisitions. The 3-ns-long gates slide in time with an interval of 250 ps. For each gate, an image is acquired. Temporal convolution of the signal with the gates results in a delay between the laser pulse (a few tens of picoseconds long) and the center of the maximal frame. Top right is the obtained decay averaged over the images. All images share the same color scale (from 3.5×10^4 to 6×10^4 counts). (b) TRPL intensity, computed as the space integration of the TRFLIM signal, as a function of time for different fluences acquired with a time shift of 250 ps. Dark curves correspond to lower fluences (down to 4×10^{11} ph cm $^{-2}$) and red curves to higher fluences (up to 10^{13} ph cm $^{-2}$). Inset, comparison of subnanosecond-resolved curves (open circles) with regular decays resolved at 3 ns (line). Only the first 150 ns of the regular and longer decay (that lasts up to $t = 879$ ns) are shown. (c) Relative slope fitted on the decays between 0.5 and 2.5 ns as a function of laser fluence: blue, measured on raw decays; yellow, measured on deconvoluted decays. Error bars are given by the fitting function; see Sec. 2 on numerical uncertainty within the Supplemental Material [34]. Curves are fitted by using a linear function (dotted line): $y = ax + b$. Parameters found for the raw scaling are $a = -(5.7 \pm 0.6) \times 10^{-6}$ cm 2 s $^{-1}$ and $b = -(1.24 \pm 0.03) \times 10^8$ s $^{-1}$. Parameters found from scalings from deconvoluted decays are $a = -(1.07 \pm 0.15) \times 10^{-5}$ cm 2 s $^{-1}$ and $b = -(2.06 \pm 0.08) \times 10^8$ s $^{-1}$.

literature results on triple-cation perovskites [35] and with our previous results [24].

This analysis can also be performed locally on images, as shown in Sec. IV and Fig. S8 within the Supplemental Material [34]. For each pixel, a binning with the neighboring pixels is performed (10×10 pixels, centered), and a linear scaling is fitted from the derivatives measured on the local deconvoluted decays. The maps of the slope and intercept of the scalings are displayed in Figs. S8(a) and S8(d) within the Supplemental Material [34]. We can observe local variations that are negatively correlated between the intercept and the slope; see Fig. S8(c) within the Supplemental Material [34]. According to our simulations, this anticorrelation can be explained by noise in the determined derivative of the decays; see Fig. S8(f) within the Supplemental Material [34]. This means that local application of the scaling law suffers from high noise on the local decays in our dataset. With such a level of local noise, we are unable to output independent maps of slope and intercept, which would lead to independent maps of material parameters.

However, one advantage of our approach over phenomenological fitting is that it allows us to form a hypothesis based on physical considerations. In the situation currently under scrutiny, we can assume that the bulk properties of the film are uniform and that heterogeneities are caused by local differences in the local top-surface recombination velocity. Under this hypothesis, all local scalings should have the same slope, since the absorption coefficient, α , and the external radiative-recombination coefficient, k_2 , are considered constant. Indeed, we evaluated the impact of the local outcoupling on the slope of scaling via a modification of the external radiative-recombination coefficient and find it to be less than the sensitivity of our technique; moreover, the outcoupling is found to have no impact on the intercept of the scaling. Therefore, under this approximation, only the intercept of the scalings should vary locally, and its variation is attributed to a variation in local surface-recombination velocity, see Eq. (7). We fix the slope of local scalings to the value we obtain from the spatially averaged decays, $a = -(1.07 \pm 0.15) \times 10^{-5} \text{ cm}^2 \text{ s}^{-1}$, and compute only the local intercept. In doing so, we obtain a map of the local intercept of scaling. By assuming values for the bulk SRH recombination parameter, k_1 , and the diffusion coefficient, D , it is possible to extract a map of the local top-surface recombination velocity, S_t , as shown in Fig. 2(a). The values we assume for D and k_1 are the results of a drift-diffusion fit of longer decays presented in Sec. IV. In Fig. 2(b), we show a vertical cross section of the map. We can see variations that are above the estimated error bars. To justify our assumption that local surface recombination is the origin of the variation of the intercept, we evaluate, from Eq. (7) and the chosen parameter set, that top-surface recombination accounts for 76% of the value of the intercept. We can thus

conclude that the scaling law, combined with the hypothesis for the material under study, allows us to observe local variations of parameters in a direct way.

To test the technique further, we perform experiments on inhomogeneous samples: perovskite on glass that was exposed to an x-ray beam. The application of the scaling-law technique is shown in Sec. IV.B and Fig. S10 within the Supplemental Material [34]. In this case, we image variations of local intercepts that correspond to the x-ray spot, while the slope of scaling shows little variation. In this inhomogeneous case, no hypothesis is required, as we find uncorrelated variations of slopes and intercepts.

IV. DISCUSSION

In this section, we discuss the obtained results. First, we comment on the values of the parameters obtained with this technique. Then, we compare this technique with regular drift-diffusion fitting, and we demonstrate that using the scaling law leads to a higher level of accuracy in the determination of parameters. Next, we discuss the validity of the assumptions leading to Eq. (7), describing the scaling law. Finally, we discuss the limits of the proposed technique and possible future improvements.

By following the scaling-law approach, we obtain a value for the external radiative-recombination coefficient, k_2 , equal to $k_2 = (1.2 \pm 0.4) \times 10^{-10} \text{ cm}^3 \text{ s}^{-1}$. According to Brenes *et al.* [35], the internal radiative-recombination coefficient of $\text{Cs}_{0.05}(\text{MA}_{0.17}\text{FA}_{0.83})_{0.95}\text{Pb}(\text{Br}_{0.17}\text{I}_{0.83})_3$ perovskite is in the order of $k_2 = 2.0 \times 10^{-10} \text{ cm}^3 \text{ s}^{-1}$, while the external radiative-recombination coefficient, evaluated by taking into account photon recycling, is in the order of $k_2^{\text{ext}} = 1.0 \times 10^{-11} \text{ cm}^3 \text{ s}^{-1}$. First, we can observe that our technique is able to yield a value close to what is expected for such materials. Second, the value we find is close to the internal radiative-recombination coefficient, as expected by our simulations of the impact of photon recycling in the present case; see Sec. I.D within the Supplemental Material [34]. The difference between the value given in Ref. [35] and ours can have different origins. One is the overall uncertainty of this parameter, which is still not determined with precision. Second, the obtained value is dependent on the measurement of the absorption coefficient at the laser wavelength, α . Third, we show that temporal convolution has an impact on the determination of the radiative coefficient. This calls for a more detailed study on the best method to deconvolute the signal and obtain the most-precise estimate. Therefore, we conclude that the scaling law allows us to extract a direct value for the external radiative-recombination coefficient, which, in the present low-photon-recycling case, is close to the internal radiative-recombination coefficient.

To ascertain the accuracy of the parameters we obtain from this measurement technique, we perform a comparison with the drift-diffusion fit of longer decays.

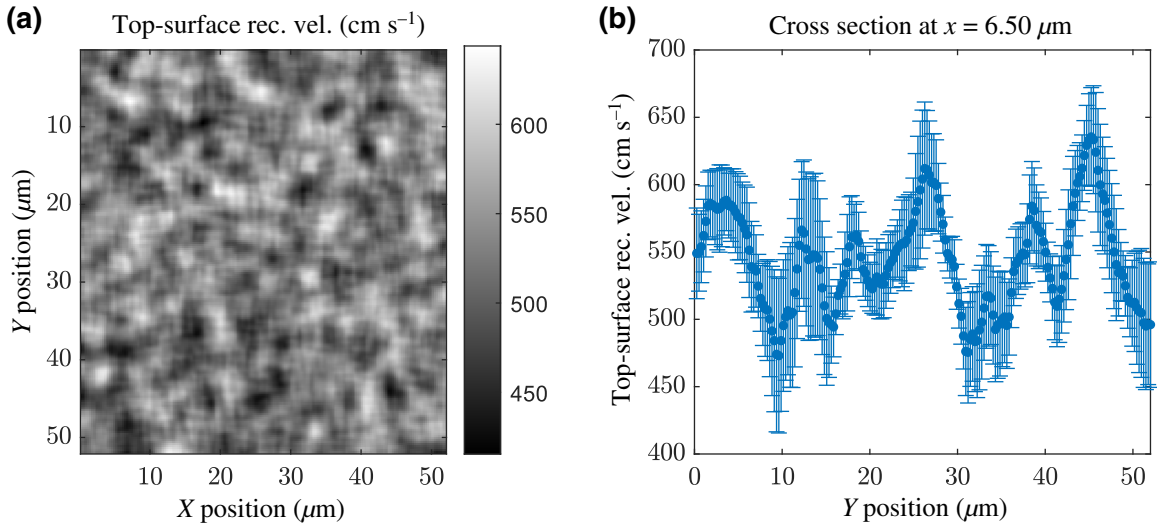


FIG. 2. Local determination of parameters. (a) Map of top-surface recombination velocity from fitted local intercepts of local scalings. Seven fluence acquisitions of Fig. 1 are used at a local scale. Binning of 10 pixels is applied, meaning that all pixels are averaged out over a square of 10×10 pixels. For each pixel, seven decays are obtained, corresponding to seven fluences. Derivative of deconvoluted decays are computed between 0.5 and 2.5 ns. Derivatives are assembled to form the scaling, from which the intercept is fitted. Slope for all points is set to $a = -1.07 \times 10^{-5} \text{ cm}^2 \text{ s}^{-1}$. To obtain the map of local intercept, we compute locally the average of the ensemble, $E = (\text{derivative} - a \times \text{fluence})$. For the uncertainty, we compute $\text{std}(E)/\sqrt{E_n}$, with E_n as the number of elements in E . Then, we use Eq. (7) and the assumed values for the other parameters to compute the map of S_{top} from the map of the intercept. Parameters are estimated to be $D = 3.54 \times 10^{-3} \text{ cm}^2 \text{ s}^{-1}$, $k_1 = 9.23 \times 10^6 \text{ s}^{-1}$, and $\alpha = 6.5 \times 10^4 \text{ cm}^{-1}$. (b) Vertical cross section of map (a) at $x = 6.5 \mu\text{m}$.

The parameter that our scaling is able to determine is the radiative-recombination coefficient, k_2 . Therefore, we implement two fitting strategies. One, in which k_2 is used as a fitting parameter, is named strategy 1, and another, where we fix k_2 to the value obtained by the scaling measurement, is named strategy 2. For both, we also fit D , k_1 , N_{bulk} , S_{top} , and N_{top} . We fit the seven TRPL curves together at once and with only one model for all the curves: no parameter is changed as a function of fluence. The results of the first fitting are presented in Fig. S6 within the Supplemental Material [34]. For strategy 2, the fitted parameters are available in Table S1 within the Supplemental Material [34], while the correlations between fitted parameters are given in Table S2 within the Supplemental Material [34]. Overall, the correlations are reasonably low. The highest correlations are between D , N_{top} , and N_{bulk} , and equal +0.78, indicating that these three parameters have similar bending effects on the decay curves.

We compare the results of the two fitting strategies: comparable values for the fitted parameters are obtained in both cases. In addition, the uncertainties of the fitted parameters are reduced when considering the value of k_2 determined by scaling (see Table S3 within the Supplemental Material [34]). In particular, the uncertainty of N_{top} goes from 42% when k_2 is a free fitting parameter to 25% when k_2 is fixed. Finally, the value of radiative recombination from the drift-diffusion fit is $k_2^{\text{DD}} = (1.16 \pm 0.07) \times 10^{-10}$, which is fully compatible with the value obtained

with scaling. Therefore, we conclude that the scaling law is complementary to regular drift-diffusion fitting.

Moreover, the experimental observation of linear scaling proves that our assumptions to obtain it are reasonable. Namely, four main assumptions lead to Eq. (7). (i) The intrinsic nature of the perovskite material, which, according to this experiment, is doped less than $3 \times 10^{16} \text{ cm}^{-3}$. In a recent study by Feldmann *et al.* [46], photodoping of the perovskite was evidenced at timescales in the order of tens of nanoseconds. Our technique is not sensitive to such effects, as it relies on the very first nanoseconds of the decays. (ii) At a short time, under our experimental conditions, one can neglect the defect-related densities, N_{bulk} and N_{top} , in front of the photogenerated carrier density; this is also confirmed by the values found for these parameters by the drift-diffusion fitting presented above. (iii) No high-order Auger-like recombination is observed, as it would lead to a term, $\propto n_v^2$, in the scaling (see the formula of the scaling in this case and a more detailed discussion in the Supplemental Material [34]). (iv) At a short time, the spatial profile of the carriers is both close to the Beer-Lambert initial condition and following the drift-diffusion equation. Short time is therefore defined as the time during which this approximation is valid.

However, we also note that our technique has two main experimental limitations. The first one is due to the camera's temporal-response function. To reduce the gap between experimental measurements and theoretical

models, we use deconvolution algorithms, as discussed above. It is worth noting that this limitation is not due to our method, but it is a common issue to all time-convoluted signals. The second one is related to the use of the scaling-law approach to map transport parameters. We observe that noise on the local decays creates a negative correlation between the intercept and the slope fitted at a local level. This renders it difficult to determine the two parameters independently at the local scale, when the variations on the sample are in the order of the sensitivity of the technique. However, the correlation could potentially also occur for physical reasons, but, to date, our measurements cannot distinguish the two. This limitation can be surpassed when hypotheses are proposed on the nature of the material under study or when the spatial variations are greater than the sensitivity.

V. CONCLUSION

We present a method for acquiring and interpreting TRPL (or TRFLIM) data from the combination of advanced modeling and characterization of intrinsic materials. This method relies on the observation of the derivative of the PL decay a short time after the laser pulse. The derivative is analyzed as a function of the laser fluence, with expected linear behavior. This scaling is obtained from a simple analytical model and applied to triple-cation lead-halide perovskites with TRFLIM measurements to investigate the transport properties. A value of the external radiative-recombination coefficient is extracted and then confirmed by a single drift-diffusion model for seven different excitation powers. Moreover, the scaling allows for the local determination of the top-surface recombination velocity under the hypothesis of spatially constant bulk properties of the thin film. Most importantly, this approach represents an important step towards more direct measurements of various physical parameters. This is crucial for the determination of the transport properties of perovskite materials, which are still under intense debate in the community. Moreover, the scaling-law technique improves classical drift-diffusion fitting, as it allows the uncertainties on the fitted parameter to be reduced.

As previously mentioned here, another set of experiments can be performed by varying the laser wavelength. This would lead to the observation of scaling as a function of the absorption coefficient, $\alpha(\lambda)$. Together with a power study, this excitation study could allow for the determination of most of the parameters without using a single drift-diffusion code. Finally, the scaling law is valid for probing short time dynamics, but it does not suffice to correctly model phenomena occurring over long times. Notably, some of the model parameters matter only at a longer timescale. This arouses our interest in the theoretical investigation of long timescale dynamics, where complementary physical information is contained.

VI. MATERIAL FABRICATION

A double-cation perovskite solution, $(\text{MA}_{0.17}\text{FA}_{0.83})\text{Pb}(\text{Br}_{0.17}\text{I}_{0.83})_3$, is prepared by dissolving 1.10-*M* PbI_2 (TCI Chemicals), 0.20-*M* PbBr_2 (Alfa Aesar), 1.00-*M* formamidinium iodide (FAI, Dyesol), and 0.20-*M* methylammonium bromide (MABr, Dyesol) in a mixture of dimethylsulfoxide (DMSO)-dimethylformamide (DMF) 1:4 in vol.-vol. as the solvent. To obtain the triple-cation perovskite, i.e., $\text{Cs}_{0.05}(\text{MA}_{0.17}\text{FA}_{0.83})_{0.95}\text{Pb}(\text{Br}_{0.17}\text{I}_{0.83})_3$, Cs^+ is additionally injected from a 1.50-*M* precursor solution of CsI (Sigma-Aldrich) in DMSO. The solution, after 2 h of stirring in a magnetic mixer, is spin-coated onto glass substrates by following a double plateau. First, 35 μL of the perovskite solution is spin-coated at a rotation of 2000 rpm for 10 s at an acceleration of 1000 rpm/s. Then, 100 μL of chlorobenzene is spin-coated at a speed of 6000 rpm for 30 s. After deposition, the perovskite films are submitted to an annealing treatment at a temperature of 100 °C for 30 min in a nitrogen glovebox. The thickness of the perovskite thin films is approximately 500 nm.

VII. EXPERIMENTAL METHODS

Wide-field illumination imaging is realized with a TRFLIM setup. The system is composed of a Talisker pulsed laser ($\lambda = 532$ nm, $f = 40$ kHz), an intensified electron-multiplied CCD camera (em-ICCD, PIMAX4, Princeton Instruments), and a home-built optomechanical excitation-collection setup. The gate width of the camera is set to 3 ns. For the subnanosecond-resolved curves, the camera gating time is varied in 250-ps steps from -5.5 to 19.5 ns. For the regular curves, the camera gating time is varied in 3-ns steps from -21 to 879 ns. Photoluminescence is collected through a Nikon 50 \times high-working-distance objective with $\text{NA} = 0.80$. The sample is placed in a cryostat chamber set at 20 °C and filled with nitrogen. The PL is filtered through short-pass and long-pass filters (DMLP650R and FES750, Thorlabs). Each acquisition is repeated 3 times in a row, with a 5-s pause in between. Acquisitions are post-treated using MATLAB.

VIII. SIMULATION METHODS

Simulations are performed using a home-made MATLAB code. The PDEPE function is used to solve the drift-diffusion equation for the photogenerated excess carrier density, Δn . This code is validated against the SILVACO Atlas simulation tool. For fitting, the convolution of the simulated decays with the apparatus-response function is performed with the phenomenological fit of the response function, see the section on deconvolution in the Supplemental Material [34]. For fitting, all seven fluence curves are fitted at once and compiled into a two-dimensional matrix of experimental data. The fitted curves are the natural logarithm of the normalized PL decays. For each curve,

only the points where the normalized PL level is greater than 5×10^{-4} are used for fitting.

ACKNOWLEDGMENTS

This project is supported by the French Government in the frame of the program of investment for the future (Programme d'Investissement d'Avenir, Grant No. ANR-IEED-002-01). S.C. would like to thank funding from the European Union's Horizon 2020 research and innovation programme under Marie Skłodowska-Curie Grant No. 845612. We declare no conflict of interest.

-
- [1] G. Kim, H. Min, K. S. Lee, D. Y. Lee, S. M. Yoon, and S. I. Seok, Impact of strain relaxation on performance of a-formamidinium lead iodide perovskite solar cells, *Science* **370**, 108 (2020).
- [2] Best Research-Cell Efficiency Chart — Photovoltaic Research — NREL, <https://www.nrel.gov/pv/cell-efficiency.html>, accessed: 2021-02-18.
- [3] H. Jin, E. Debroye, M. Keshavarz, I. G. Scheblykin, M. B. J. Roeffaers, J. Hofkens, and J. A. Steele, It's a trap! on the nature of localised states and charge trapping in lead halide perovskites, *Mater. Horiz.* **7**, 397 (2020).
- [4] S. Reichert, Q. An, Y. W. Woo, A. Walsh, Y. Vaynzof, and C. Deibel, Probing the ionic defect landscape in halide perovskite solar cells, *Nat. Commun.* **11**, 1 (2020).
- [5] S. G. Motti, T. Crothers, R. Yang, Y. Cao, R. Li, M. B. Johnston, J. Wang, and L. M. Herz, Heterogeneous photon recycling and charge diffusion enhance charge transport in quasi-2D lead-halide perovskite films, *Nano Lett.* **19**, 11 (2019).
- [6] P. Schulz, D. Cahen, A. Kahn, and Halide Perovskites, Is it all about the interfaces?, *Chem. Rev.* **119**, 3349 (2019).
- [7] J. Wang, W. Fu, S. Jariwala, I. Sinha, A. K. Jen, and D. S. Ginger, Reducing surface recombination velocities at the electrical contacts will improve perovskite photovoltaics, *ACS Energy Lett.* **4**, 222 (2019).
- [8] S. Cacovich, D. Messou, A. Bercegol, S. Béchu, A. Yaiche, H. Shafique, J. Rousset, P. Schulz, M. Bouttemy, and L. Lombez, Light-induced passivation in triple cation mixed halide perovskites: Interplay between transport properties and surface chemistry, *ACS Appl. Mater. Interfaces* **12**, 34784 (2020).
- [9] M. Khenkin, E. Katz, and A. E. A. Abate, Consensus statement for stability assessment and reporting for perovskite photovoltaics based on ISOS procedures, *Nat. Energy* **5**, 35 (2020).
- [10] G. Delport, S. Macpherson, and S. D. Stranks, Imaging carrier transport properties in halide perovskites using time-resolved optical microscopy, *Adv. Energy Mater.* **10**, 1903814 (2020).
- [11] W. Chen, Z. Gan, M. A. Green, B. Jia, and X. Wen, Revealing dynamic effects of mobile ions in halide perovskite solar cells using time-resolved microspectroscopy, *Small Methods* **5**, 2000731 (2021).
- [12] E. M. Hutter, T. Kirchartz, B. Ehrler, D. Cahen, and E. v. Hauff, Pitfalls and prospects of optical spectroscopy to characterize perovskite-transport layer interfaces, *Appl. Phys. Lett.* **116**, 100501 (2020).
- [13] D. W. Dequillettes, K. Frohna, D. Emin, T. Kirchartz, V. Bulovic, D. S. Ginger, and S. D. Stranks, Charge-Carrier Recombination in Halide Perovskites (2019).
- [14] D.-Y. Son, J.-W. Lee, Y. J. Choi, I.-H. Jang, S. Lee, P. J. Yoo, H. Shin, N. Ahn, M. Choi, D. Kim, and N.-G. Park, Self-formed grain boundary healing layer for highly efficient CH₃NH₃PbI₃ perovskite solar cells, *Nat. Energy* **1**, 1 (2016).
- [15] D. W. Dequillettes, S. M. Vorpahl, S. D. Stranks, H. Nagaoka, G. E. Eperon, M. E. Ziffer, H. J. Snaith, and D. S. Ginger, Impact of microstructure on local carrier lifetime in perovskite solar cells, *Science* **348**, 683 (2015).
- [16] T. Yamada, Y. Yamada, Y. Nakaike, A. Wakamiya, and Y. Kanemitsu, Photon Emission and Reabsorption Processes in CH₃NH₃PbBr₃ Single Crystals Revealed by Time-Resolved Two-Photon-Excitation Photoluminescence Microscopy, *Phys. Rev. Appl.* **7**, 014001 (2017).
- [17] M. Zhang, H. Yu, M. Lyu, Q. Wang, J. H. Yun, and L. Wang, Composition-dependent photoluminescence intensity and prolonged recombination lifetime of perovskite CH₃NH₃PbBr_{3-x}Cl_xfilms, *Chem. Commun.* **50**, 11727 (2014).
- [18] R. K. Ahrenkiel and M. Lundstrom, *Minority Carriers in III-V Semiconductors: Physics and Applications, Semiconductors and Semimetals*, Vol. 39 (Academic Press, Incorporated, 1993), p. 39.
- [19] A. A. Baloch, F. H. Alharbi, G. Grancini, M. I. Hossain, M. K. Nazeeruddin, and N. Tabet, Analysis of photocarrier dynamics at interfaces in perovskite solar cells by time-resolved photoluminescence, *J. Phys. Chem. C* **122**, 26805 (2018).
- [20] T. Kirchartz, J. A. Márquez, M. Stolterfoht, and T. Unold, Photoluminescence-based characterization of halide perovskites for photovoltaics, *Adv. Energy Mater.* **10**, 1904134 (2020).
- [21] M. Maiberg and R. Scheer, Theoretical study of time-resolved luminescence in semiconductors. II. Pulsed excitation, *J. Appl. Phys.* **116**, 123711 (2014).
- [22] M. J. Trimpl, A. D. Wright, K. Schutt, L. R. V. Buizza, Z. Wang, M. B. Johnston, H. J. Snaith, P. Müller-Buschbaum, and L. M. Herz, Charge-carrier trapping and radiative recombination in metal halide perovskite semiconductors, *Adv. Funct. Mater.* **30**, 2004312 (2020).
- [23] A. Bercegol, S. Cacovich, G. Vidon, S. Mejaouri, A. Yaiche, J. B. Puel, C. Longeaud, J. F. Guillemoles, S. Juttau, J. Rousset, D. Ory, and L. Lombez, Imaging electron, hole, and ion transport in halide perovskite, *J. Phys. Chem. C* **124**, 11741 (2020).
- [24] A. Bercegol, F. J. Ramos, A. Rebai, T. Guillemot, D. Ory, J. Rousset, and L. Lombez, Slow diffusion and long lifetime in metal halide perovskites for photovoltaics, *J. Phys. Chem. C* **122**, 24570 (2018).
- [25] A. Bercegol, D. Ory, D. Suchet, S. Cacovich, O. Fournier, J. Rousset, and L. Lombez, Quantitative optical assessment of photonic and electronic properties in halide perovskite, *Nature Communications* (2019).
- [26] A. Sridharan, N. K. Noel, B. P. Rand, and S. Kéna-Cohen, Role of photon recycling and band filling in halide perovskite photoluminescence under

- focussed excitation conditions, *J. Phys. Chem. C* **125**, 2240 (2021).
- [27] T. P. Weiss, B. Bissig, T. Feurer, R. Carron, S. Buecheler, and A. N. Tiwari, Bulk and surface recombination properties in thin film semiconductors with different surface treatments from time-resolved photoluminescence measurements, *Sci. Rep.* **9**, 5385 (2019).
- [28] B. Krogmeier, F. Staub, D. Grabowski, U. Rau, and T. Kirchartz, Quantitative analysis of the transient photoluminescence of CH₃NH₃PbI₃/PC61BM heterojunctions by numerical simulations, *Sustainable Energy and Fuels* **2**, 1027 (2018).
- [29] M. Saba, M. Cadelano, D. Marongiu, F. Chen, V. Sarritzu, N. Sestu, C. Figus, M. Aresti, R. Piras, A. Geddo Lehmann, C. Cannas, A. Musinu, F. Quochi, A. Mura, and G. Bongiovanni, Correlated electron-hole plasma in organometal perovskites, *Nat. Commun.* **5**, 1 (2014).
- [30] A. Kanevce, D. H. Levi, and D. Kuciauskas, The role of drift, diffusion, and recombination in time-resolved photoluminescence of CdTe solar cells determined through numerical simulation, *Prog. Photovoltaics: Res. Appl.* **22**, 1138 (2014).
- [31] P. Würfel, *Physics of Solar Cells* (Wiley, 2005).
- [32] W. Shockley and W. T. Read, Statistics of the recombinations of holes and electrons, *Phys. Rev.* **87**, 835 (1952).
- [33] R. N. Hall, Electron-hole recombination in germanium [21] (1952).
- [34] See the Supplemental Material at <http://link.aps.org/supplemental/10.1103/PhysRevApplied.16.044058> for additional theoretical and experimental details.
- [35] R. Brenes, M. Laitz, J. Jean, D. W. deQuilettes, and V. Bulović, Benefit from Photon Recycling at the Maximum-Power Point of State-Of-The-Art Perovskite Solar Cells, *Phys. Rev. Appl.* **12**, 14017 (2019).
- [36] L. M. Pazos-Outón, M. Szumilo, R. Lamboll, J. M. Richter, M. Crespo-Quesada, M. Abdi-Jalebi, H. J. Beeson, M. Vrućinić, M. Alsari, H. J. Snaith, B. Ehrler, R. H. Friend, and F. Deschler, Photon recycling in lead iodide perovskite solar cells, *Science* **351**, 1430 (2016).
- [37] J. M. Richter, M. Abdi-Jalebi, A. Sadhanala, M. Tabachnyk, J. P. Rivett, L. M. Pazos-Outón, K. C. Gödel, M. Price, F. Deschler, and R. H. Friend, Enhancing photoluminescence yields in lead halide perovskites by photon recycling and light out-coupling, *Nat. Commun.* **7**, 1 (2016).
- [38] M. Ansari-Rad and J. Bisquert, Insight Into Photon Recycling in Perovskite Semiconductors from the Concept of Photon Diffusion, *Phys. Rev. Appl.* **10**, 034062 (2018).
- [39] T. Handa, D. M. Tex, A. Shimazaki, A. Wakamiya, and Y. Kanemitsu, Charge injection mechanism at heterointerfaces in CH₃NH₃PbI₃ perovskite solar cells revealed by simultaneous time-resolved photoluminescence and photocurrent measurements, *J. Phys. Chem. Lett.* **8**, 954 (2017).
- [40] J. Haddad, B. Krogmeier, B. Klingebiel, L. Krückemeier, S. Melhem, Z. Liu, J. Hüpkens, S. Mathur, and T. Kirchartz, Analyzing interface recombination in lead-halide perovskite solar cells with organic and inorganic hole-transport layers, *Adv. Mater. Interfaces* **7**, 2000366 (2020).
- [41] D. Głowienka, D. Zhang, F. Di Giacomo, M. Najafi, S. Veenstra, J. Szmytkowski, and Y. Galagan, Role of surface recombination in perovskite solar cells at the interface of HTL/CH₃NH₃PbI₃, *Nano Energy* **67**, 104186 (2020).
- [42] H. J. Lin, S. Cacovich, A. Rebai, J. Rousset, and C. Longeaud, Influence of environment and light-stress on the optoelectronic properties of triple-cation perovskite thin films, *ACS Appl. Mater. Interfaces* **12**, 19495 (2020).
- [43] J. Holovský, S. De Wolf, J. Werner, Z. Remeš, M. Müller, N. Neykova, M. Ledinský, L. Černá, P. Hrzina, P. Löper, B. Niesen, and C. Ballif, Photocurrent spectroscopy of perovskite layers and solar cells: A sensitive probe of material degradation, *J. Phys. Chem. Lett.* **8**, 838 (2017).
- [44] P. Löper, M. Stuckelberger, B. Niesen, J. Werner, M. Filipič, S. J. Moon, J. H. Yum, M. Topič, S. De Wolf, and C. Ballif, Complex refractive index spectra of CH₃NH₃PbI₃ perovskite thin films determined by spectroscopic ellipsometry and spectrophotometry, *J. Phys. Chem. Lett.* **6**, 66 (2015).
- [45] E. V. Péan, C. S. De Castro, and M. L. Davies, Shining a light on the photoluminescence behaviour of methylammonium lead iodide perovskite: Investigating the competing photobrightening and photodarkening processes, *Mater. Lett.* **243**, 191 (2019).
- [46] S. Feldmann, S. Macpherson, S. P. Senanayak, M. Abdi-Jalebi, J. P. H. Rivett, G. Nan, G. D. Tainter, T. A. S. Doherty, K. Frohna, E. Ringe, R. H. Friend, H. Sirringhaus, M. Saliba, D. Beljonne, S. D. Stranks, and F. Deschler, Photodoping through local charge carrier accumulation in alloyed hybrid perovskites for highly efficient luminescence, *Nat. Photonics* **14**, 123 (2019).